Ceramics International xxx (xxxx) xxx–xxx

Contents lists available at ScienceDirect

Ceramics International

journal homepage: www.elsevier.com/locate/ceramint

Effects of $(Cr_{0.5}Ta_{0.5})^{4+}$ on structure and microwave dielectric properties of $Ca_{0.61}Nd_{0.26}TiO_3$ ceramics

Zhe Xiong[a], Bin Tang[a,*], Zixuan Fang[a,b], Chengtao Yang[a], Shuren Zhang[a]

[a] National Engineering Research Center of Electromagnetic Radiation Control Materials, University of Electronic Science and Technology of China, Chengdu 611731, China
[b] Department of Material Science and Engineering, University of California, Berkeley, United States

ARTICLE INFO

Keywords:
Microwave ceramics
Substitution
Crystal structure
Raman spectroscopy

ABSTRACT

The $Ca_{0.61}Nd_{0.26}Ti_{1-x}(Cr_{0.5}Ta_{0.5})_xO_3$ (CNT-CT*x*) ceramics with orthorhombic perovskite structure were prepared using the conventional solid-state method. The X-ray diffraction (XRD), Raman spectra and X-ray photoelectron spectra (XPS) were employed to investigate the correlations between crystal structure and microwave dielectric properties of CNT-CT*x* ceramics. The XRD results showed that all CNT-CT*x* samples were crystallized into the orthorhombic perovskite structure. The SEM micrographs indicated that the average grain size of samples depended on the sintering temperature. As $(Cr_{0.5}Ta_{0.5})^{4+}$ concentration increased, there was a significant decrease in the average grain size of samples. The short range order (SRO) structure and structural distortion of oxygen octahedra proved to exist in CNT-CT*x* crystals according to the analysis of Raman spectra results. The microwave dielectric properties highly depended on the full width at half maximum (FWHM) of Raman spectra, oxygen octahedra distortion, reduction of Ti^{4+} to Ti^{3+} and bond valence. At last, the CNT-CT0.05 ceramic sintered at 1420 °C for 4 h exhibited the good and stable comprehensive microwave dielectric properties: relative permittivity of 96.5, quality factor of 14,360 GHz, and temperature coefficient of resonant frequency of +153.3 ppm/°C.

1. Introduction

There is a great demand for microwave dielectric ceramics with excellent properties to meet the high criteria of microwave device in the fields of global positioning system (GPS), wireless local area network (WLAN) technology and ceramic substrate materials [1–4]. Thus, the request of higher microwave dielectric properties is raised to satisfy the characteristic of miniaturization, integration and prominent frequency selectivity and stability of microwave components, such as the desirable relative permittivity (ε_r), high quality factor ($Q \times f$) and near zero temperature coefficient of resonant frequency (τ_f) [5].

To date, the Calcium and Neodymium-based perovskite ceramics have attracted many attentions owing to their good performance in relative permittivity and dielectric loss. Particularly, the $Ca_{0.61}Nd_{0.26}TiO_3$ (CNT) ceramics are promising to be a suitable microwave dielectric material with $\varepsilon_r \sim 108$, $Q \times f \sim 17{,}200$ GHz, and $\tau_f \sim +270$ ppm/°C [6], but its large positive τ_f value is too high to be practically utilized in microwave device. Therefore, it is necessary to obtain a microwave dielectric ceramic material of nero-zero τ_f by taking some effective measures. Combining two or more ceramics with completely opposite τ_f value is a promising and effective way to tune the τ_f value. For example, Chen et al. [7] have investigated the microwave dielectric properties and microstructures of $Ca_{1-x}Nd_{2x/3}TiO_3$-$Li_{0.5}Nd_{0.5}TiO_3$ ceramics, and found that the $0.55Ca_{0.61}Nd_{0.26}TiO_3$-$0.45(Li_{0.5}Nd_{0.5})TiO_3$ ceramics had optimum microwave dielectric properties of $\varepsilon_r \sim 101$, $Q \times f \sim 5300$ GHz, and $\tau_f \sim +13$ ppm/°C. The $0.55Ca_{0.6}Nd_{0.8/3}TiO_3$-$0.45(Li_{0.5}Nd_{0.5})TiO_3$ + 0.03Li ceramics were synthesized at 1190 °C by Zhou et al. [8], and had single orthorhombic perovskite structure, together with the optimum microwave dielectric properties of $\varepsilon_r = 129$, $Q \times f = 3600$ GHz, $\tau_f = +38$ ppm/°C. Moreover, noncubic complex perovskite $Nd(Zn_{0.5}Ti_{0.5})O_3$ [9] and $Nd(Mg_{0.5}Ti_{0.5})O_3$ [10] ceramics were synthesized with monoclinic $P2_1/n$ space group and negative τ_f value of −49 ppm/°C and extremely high $Q \times f$ product of 45,000 GHz. Hence, a new ceramic system $0.4Nd(Zn_{0.5}Ti_{0.5})O_3$-$0.6Ca_{0.61}Nd_{0.26}TiO_3$ ($\varepsilon_r = 56.3$, $Q \times f = 54{,}400$ GHz, $\tau_f = +0.3$ ppm/°C) with a near-zero τ_f were obtained [11]. Hu et al. [12] pointed out that temperature compensated τ_f value (1-*x*)$Ca_{0.61}Nd_{0.26}TiO_3$-*x*$Nd(Mg_{0.5}Ti_{0.5})O_3$ + 1 *wt* % CuO ceramics could be achieved in the range of $0.3 < x < 0.5$.

Many considerations have been given to the partial substitution of the Ti^{4+} ion for B-site ions to reduce positive τ_f values in ABO_3 perovskite materials besides combining two or more compounds with negative τ_f value, such as $Ca_{0.6}La_{0.8/3}(Sn_xTi_{1-x})O_3$ [13], $(Sr_{0.2}Ca_{0.488}Nd_{0.208})Ti_{1-x}Ga_{4x/3}O_3$ [14] and $0.2SrTiO_3$-

* Corresponding author.
E-mail address: tangbin.uestc@gmail.com (B. Tang).

https://doi.org/10.1016/j.ceramint.2018.01.207
Received 11 November 2017; Received in revised form 15 January 2018; Accepted 25 January 2018

$0.8Ca_{0.61}Nd_{0.26}Ti_{1-x}Al_{4x/3}O_3$ [15] complex perovskites. Also, Moon et al. [16] and Liang et al. [17] suggested that the τ_f value could be tuned effectively by the substitution of B-site ions, which satisfy the condition that radius of B-site ions are similar radius of another kind of ions. Similarly, the ionic radius of Cr^{3+} (0.615 Å, CN = 6) and Ta^{5+} (0.64 Å, CN = 6) is close to that of Ti^{4+} (0.605 Å, CN = 6) [18]. Consequently, the aim of this work is to investigate correlations between the crystal structure, microstructures and microwave dielectric properties of $Ca_{0.61}Nd_{0.26}Ti_{1-x}(Cr_{0.5}Ta_{0.5})_xO_3$ (CNT-CT*x*) ceramics.

2. Experimental procedures

2.1. Preparation of CNT-CTx

The $CaCO_3$ (≥ 99.0%, Shantou Xilong Chemical Factory, Shantou, China), Cr_2O_3 (≥ 99.0%, Chengdu Kelong Chemical Co., Ltd, Chengdu, China), Nd_2O_3 (≥ 99.0%, Guangdong Zhujiang Rare-earth Co. Ltd., Zhujiang, China), Ta_2O_5 (≥ 99.5%, Sinopharm Chemical Reagent Co., Ltd., Shanghai, China) and TiO_2 (≥ 99.0%, Xiantao ZhongXing Electric Co., Ltd, Xiantao, China) powders were used as starting materials and weighed according to the ratio of $Ca_{0.61}Nd_{0.26}Ti_{1-x}(Cr_{0.5}Ta_{0.5})_xO_3$ (CNT-CT*x*) where x = 0, 0.025, 0.05, 0.075, 0.1, 0.125, and milled mixed by grinding with ZrO_2 balls in deionized water for 7 h. The resulting mixtures were calcined at 1130 °C for 5 h in air with 3 °C/min heating rate. Then these calcined powders were reground for 2 h, dried, mixed with a 7 wt% of a 10% solution of polyvinyl alcohol as an organic binder and homogeneously granulated in an agate mortar and pestle. The obtained powder was axially pressed into cylindrical disks with a thickness of 7 mm and a diameter of 15 mm under a pressure of 200 MPa. At last, the samples were preheated at 600 °C for 2 h to exclude the organic binder, and sintered at 1360–1450 °C for 4 h in air.

2.2. Characterization

After sintering, the bulk densities (ρ_{bul}) of samples were measured by the Archimedes method. A knowledge of the crystal structure of a ceramic permits computation of its theoretical density ρ_{tho} through the relationship: $\rho_{tho} = nA_{ato}/V_CN_A$, where n is the number of atoms associated with each unit cell; A is atomic weight; V_C is the volume of the unit cell obtained from Rietveld analysis; N_A is the Avogadro's number (6.023×10^{23} atoms/mol). Hence, the relative density was calculated using this formula: $\rho_{rel} = \rho_{bul} / \rho_{tho} \times 100\%$. The phase's identification was carried out by XRD using CuKα radiation (Philips x'pert Pro MPD, Netherlands). The visualization of crystal structure of ceramics was acquired by VESTA software with ceramics crystallography data. The refinement of crystal unit cell parameters of samples was calculated by analyzing XRD data using the "maud" based on the Rietveld method. And the microstructures of CNT-CT*x* ceramics were characterized by scanning electron microscope (SEM) (FEI Inspect F, United Kingdom). The Raman spectra were recorded at room temperature using a Raman spectrometer (RENISHAW, London, UK) with the existing line at 514 nm of a He-Ne laser at room temperature, and collected in the range of 100–1000 cm^{-1}. Besides, the Raman bands were fitted by the Lorentzian model using PeakFit software. The ε_r and $Q \times f$ values of polished samples at 3–4.5 GHz were measured with the TE011 shielded cavity reflection method with a network analyzer a network analyzer (Agilent Technologies E5071C, San Diego, CA, USA). The τ_f of specimens was determined from the difference between the resonant frequency (2–3 GHz) obtained at 25 °C and 85 °C using the Eq. (1):

$$\tau_f = \frac{\Delta f}{f_0 \cdot \Delta t} \times 10^6 = \frac{f_{85\,^\circ C} - f_{25\,^\circ C}}{f_{25\,^\circ C} \times (85 - 25)} \times 10^6 \quad (\text{ppm}/^\circ C) \tag{1}$$

In the Eq. (1), $f_{25\,^\circ C}$ and $f_{85\,^\circ C}$ represent the resonant frequency at 85 °C and 25 °C, respectively. X-ray photoelectron spectroscopy (XPS) analysis was done using the Al Kα (nonmonochromatic) radiation of an Escalab 250Xi (Thermo Fisher Scientific) spectrometer operated in the fixed analyzer transmission, and scanning step is 0.1 eV. Additionally, the tolerance factor (t) was calculated using the following equations:

$$t = \frac{\overline{R_A} + R_O}{\sqrt{2}\,(\overline{R_B} + R_O)} \tag{2}$$

Here, $\overline{R_A}$ and $\overline{R_B}$ are the average ionic radii of the ions in A-sites and also in B-site, and R_O is oxygen ionic radii. From bond-valence model, the bond valence of B-site atom in oxygen octahedra was calculated using Eqs. (3) and (4) [19].

$$v_{ij} = \exp\left(\frac{R_{ij} - d_{ij}}{B}\right) \tag{3}$$

$$V_i = \sum_j v_{ij} \tag{4}$$

where R_{ij} is the bond valence parameter, which has been tabulated based on plenty of experiment data, d_{ij} is the bond length between atom i and j, and B is an empirically determined universal constant with a value of 0.37. In order to explain the variation in the quality factor of CNT-CT*x* compositions, the packing fractions were calculated using this formula:

$$\text{Packing fraction}(\%) = \frac{volume\ of\ the\ ions\ in\ the\ cell}{volume\ of\ unit\ cell} \times Z = \frac{\frac{4}{3}\pi \times [r_{Ca}^3 \times 0.61 + r_{Nd}^3 \times 0.26 + r_{Ti}^3 \times (1-x) + x/2 \times (r_{Cr}^3 + r_{Ta}^3) + r_O^3 \times 3]}{V_{cell}} \times 4 \tag{5}$$

where r_{Ca}, r_{Nd}, r_{Ti}, r_{Cr}, r_{Ta} and r_O represent the ionic radii of Ca^{2+}, Nd^{3+} Ti^{4+}, Cr^{3+}, Ta^{5+}, and O^{2-}, respectively. Z equals 4 for CNT-CT*x* ceramics.

3. Results and discussion

3.1. Crystalline structure and microstructure

Fig. 1(a) shows XRD diffractograms of CNT-CT*x* (x = 0, 0.025, 0.05, 0.075, 0.1, 0.125) ceramics sintered at 1420 °C for 4 h. For x = 0, 0.025, 0.05, 0.075, 0.1, all reflection peaks were well indexed as orthorhombic perovskite structure in the space group of *Pnma* (62) (88–0082), and this indicated that $(Cr_{0.5}Ta_{0.5})^{4+}$ substitution did not change the major phase composition of the CNT ceramic. But as shown in Fig. 1(a), a small amount of Ta_2O_5, $Nd_2Ti_2O_7$ and new unknown phase can be detected for x = 0.125. The formation of these Ta_2O_5, $Nd_2Ti_2O_7$ and unknown phase may be due to a different chemical behavior between Ti and Cr/Ta at B-site in CNT-CT*x* samples. Fig. 1(b) depicts that the diffraction peaks for (121) lattice plane shifted towards the lower angle with the increase of x value. In addition, the refined unit cell parameters of all samples are presented in Table 1. According to Shannon ionic radii table [18], the ionic radius of Cr^{3+} (0.615 Å, CN = 6) and Ta^{5+} (0.64 Å, CN = 6) is larger than the ionc radius of Ti^{4+} (0.605 Å, CN = 6). Therefore, the substitution of $(Cr_{0.5}Ta_{0.5})^{4+}$ for Ti^{4+} led to the increase of unit cell volume according to the Bragg's law ($2d\sin\theta = n\lambda$).

The tolerance factor (t) of CNT-CT*x* ceramics is calculated from Eq. (2) and results are listed in Table 1. The substitution of $(Cr_{0.5}Ta_{0.5})^{4+}$ for Ti^{4+} caused the tolerance factor (t) of ceramics decreasing from 0.787 to 0.7865 as the x value increased. It is reported that a lower tolerance factor means a low symmetry for the material, and similar phenomena can be readily found for simple perovskites, such as $SrTiO_3$

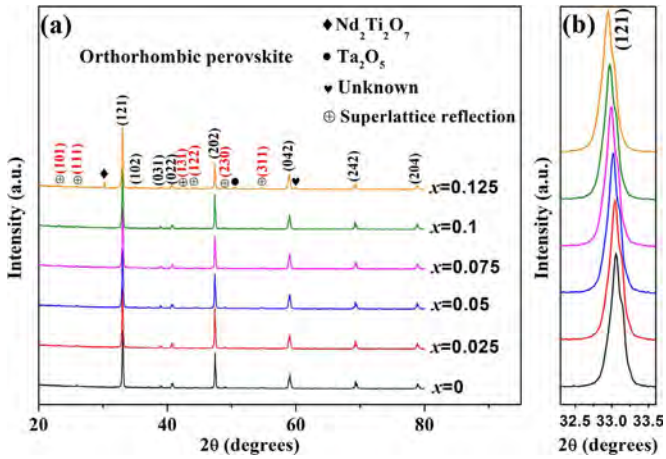

Fig. 1. (a) XRD patterns of CNT-CT*x* ceramics sintered at 1420 °C for 4 h, (b) the characteristic peaks of (121) for CNT-CT*x* phase of corresponding samples.

(t = 1.00) and $CaTiO_3$ (t = 0.98) by decreasing the tolerance factor [20]. Furthermore, Glazer [21,22] has reported that the apparent lowering of the symmetry in perovskites often results from tilting of the octhedra. For all the investigated samples, a series of extra weak peaks (marked by red color) are shown in Fig. 1(a), indicating that tilted oxygen octahedra around Ti^{4+} in the CNT system are detected in the XRD patterns. According to Glazer's theory [21], the distortion from an ideal cubic unit cell in the present system could be revealed by the indexations with combined odd (o) and even (e) Miller indices. The antiphase and in-phase BO_6 octahedral tilting (oxygen atoms coordinated displacements) in ABO_3 perovskite network without rigid distortion of the octahedron itself resulted in (ooo) reflections and (ooe), (oeo), and (eoo) reflections, respectively. And antiparallel A-site cation displacements corresponded to (eeo, eoe, and oee) combinations. So the (111), (131) and (311) super-reflections were due to the antiphase tilting of oxygen octahedra, while the (101) reflections were assigned to the in-phase tilting. Also, the (122) and (230) reflections represented the antiparallel displacement of Ca^{2+}/Nd^{3+} cations from the original positions in an ideal perovskite. The tilting mechanism defined by the present combination of the distortions is consistent with the orthorhombic $a^-a^-b^+$ tilt system with space group *Pnma* (62) based on Glazer's notation [22]. Fig. 2 describes the representative schematic illustration of CNT ceramics with typical orthorhombic perovskite crystal structure. The conterminal oxygen octahedra tilted in the opposite direction along the pseudo-cubic [100] and [001] axes but in the same direction along the [010] axis, which illustrated the $a^-a^-b^+$ tilting system visually.

The SEM micrographs of CNT ceramics sintered at different temperatures for 4 h are shown in Fig. 3. The average grain size of CNT-CT*x* ceramics was calculated using the software of Nano Measurer (version = 1.2), and results are presented in Figs. 3 and 4. Obviously, the average grain size increased from 5.13 μm to 16.49 μm when temperature increased from 1360 °C to 1420 °C, but it did not change with further increase of the sintering temperature. For samples sintered at higher temperature (1420 °C and 1450 °C), although the average grain size was in the range of 10.7–16.49 μm, samples mainly showed large grains with grain size in excess of 100 μm. This finding suggested that the grain size of CNT-CT*x* ceramics was sensitive to the sintering temperature. Fig. 4 shows the SEM photographs of CNT-CT*x* ceramics sintered at 1420 °C for 4 h. As illustrated, the average grain size monotonously decreased from 16.49 μm at x = 0 to 2.79 μm at x = 0.125. It is reported by many studies that ion doping in ceramics with perovskite structure would reduce the grain size, such as Nb doped $BaTiO_3$ [23], Cr doped $Pb(Zn_{1/3}Nb_{2/3})_{0.2}(Zr_{0.5}Ti_{0.5})_{0.8}O_3$ [24], and Nb/Al doped $Pb(Zr,Ti)O_3$ [25]. Moreover, it turned out that Ta inhibited the grain growth in orthorhombic structure of $Zn_{0.5}Ti_{0.5}NbO_4$ [26]. Hence, it was considered that the Cr or Ta inhibited the grain growth in our samples.

The EDX was employed to study element compositions of marked grains (A–F), as shown in Fig. 4, and the collected data of EDX are listed in Table 2. According to Fig. 4(A) and EDX analysis, the typically big grain with size of over 100 μm was confirmed as $Ca_{0.61}Nd_{0.26}TiO_3$ phase. Also, the element ratio data powerfully affirmed that $(Cr_{1/2}Ta_{1/2})^{4+}$ successfully substituted for Ti^{4+}. When the concentration of $(Cr_{1/2}Ta_{1/2})^{4+}$ increased to 0.125, $Nd_2Ti_2O_7$ phase was observed by SEM (as shown in Fig. 4(E)), which was consistent with XRD results.

Table 1
Experimental unit cell parameters, tolerance factor, packing fraction and molecular polarizability (α_m) versus composition in CNT-CT*x* ceramics sintered at 1420 °C for 4 h.

x (mol)	0	0.025	0.05	0.075	0.1	0.125
a (Å)	5.4387	5.4389	5.4392	5.4390	5.4393	5.4395
b (Å)	7.6671	7.6672	7.6677	7.6681	7.6682	7.6684
c (Å)	5.4084	5.4078	5.4079	5.4083	5.4084	5.4088
V (Å^3)	225.5252	225.5310	225.5427	225.5642	225.5836	225.6117
Tolerance factor (*t*)	0.7870	0.7869	0.7868	0.7867	0.7866	0.7865
Packing fraction (%)	77.6650	77.6674	77.6687	77.6661	77.6642	77.6593
α_m	12.1902	12.1942	12.1982	12.2022	12.2062	12.2102

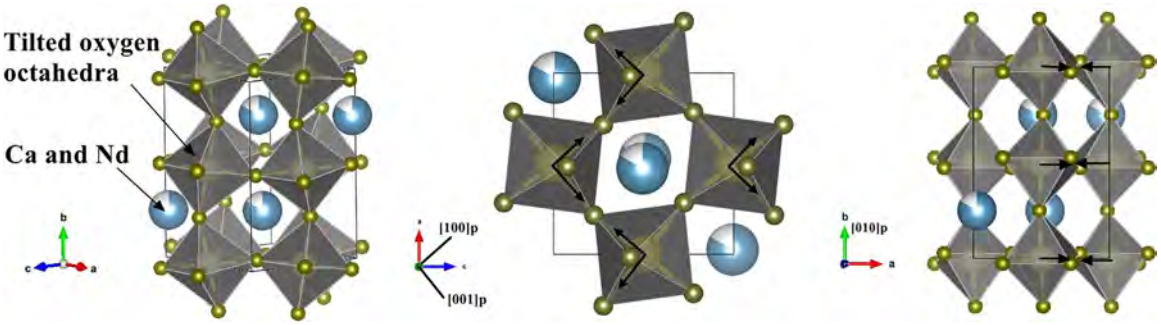

Fig. 2. Crystal structure of CNT ceramic drawn with VESTA.

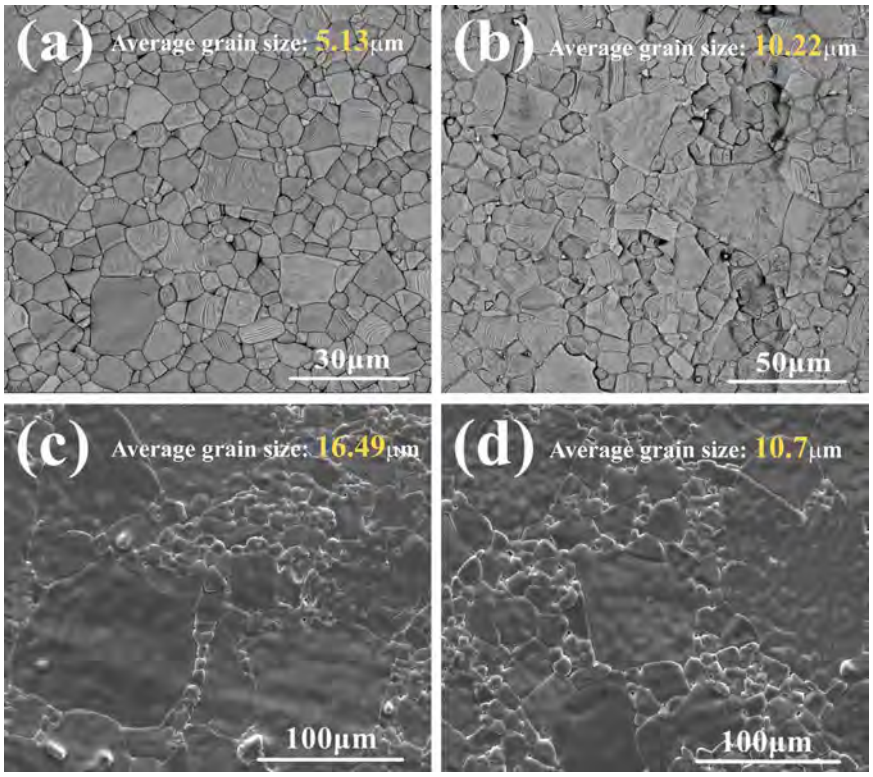

Fig. 3. SEM photographs of CNT ceramics sintered at different temperatures for 4 h with (a) 1360 °C; (b) 1390 °C; (c) 1420 °C; (d) 1450 °C.

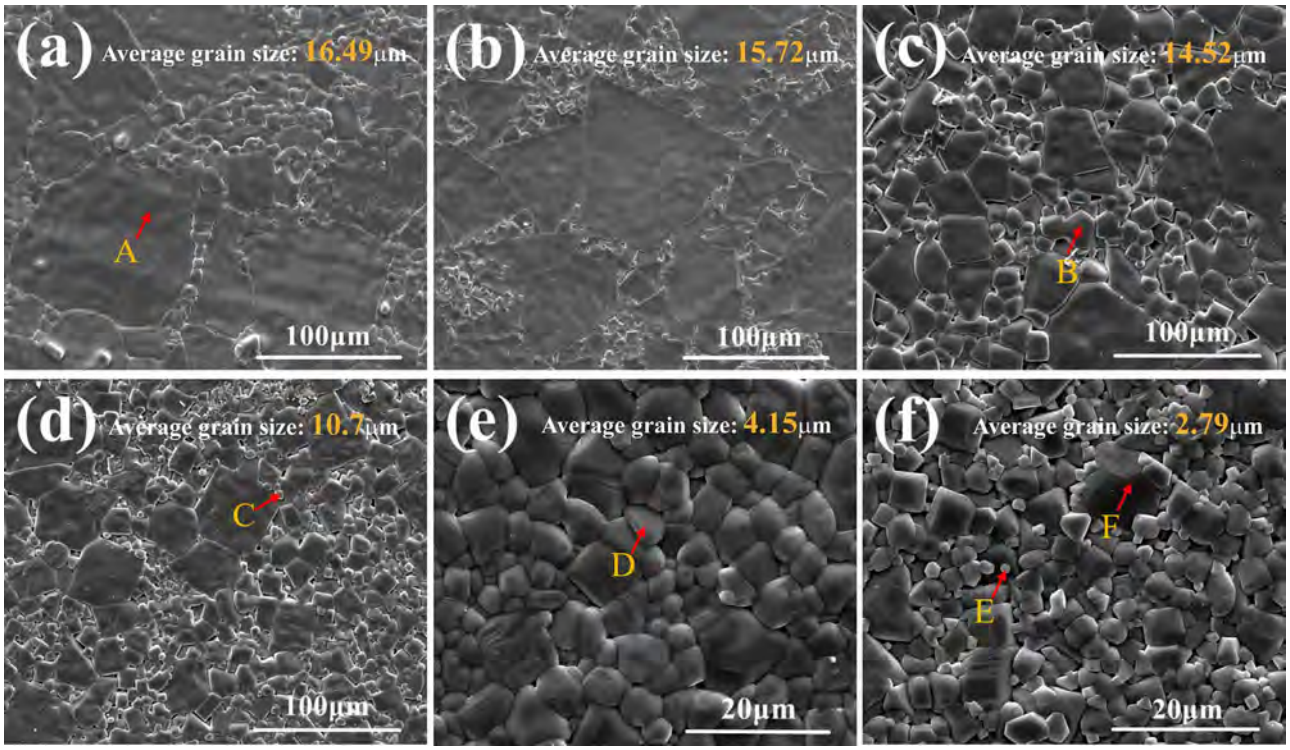

Fig. 4. SEM photographs of CNT-CT*x* ceramics sintered at 1420 °C for 4 h with (a) $x = 0$; (b) $x = 0.025$; (c) $x = 0.05$; (d) $x = 0.075$; (e) $x = 0.1$; (f) $x = 0.125$.

3.2. Raman spectra study

The Raman spectra was utilized to better understand the relationship between crystal structures and microwave dielectric properties. According to group theory, the 24 Raman active modes ($7A_g$, $7B_{1g}$, $5B_{2g}$, $5B_{3g}$) can be calculated for the $a^-a^-b^+$ tilting perovskite with orthorhombic *Pnma* (62) space group predicted [27]. However, in reality, not all of these bands can be observed, and this discrepancy was for the reason that the net change in the polarizability, or dipole moment of the vibrational mode may not be strong enough to give rise to observable Raman modes [28,29].

Fig. 5(a) shows the Raman spectra of CNT-CT*x* ceramics at room temperature of 25 °C. The spectra were similar to those for other $CaTiO_3$-based materials in many previous investigations [30–33]. As

Table 2
The EDX data of CNT-CT*x* ceramics marked grains corresponding to Fig. 4.

Spot	Atom (%)					
	Ca	Nd	Ti	Cr	Ta	O
A	12.96	5.11	21.42	0	0	60.51
B	13.52	5.73	20.11	0.46	0.55	59.63
C	12.45	5.29	19.64	0.64	0.78	61.2
D	13.19	5.82	19.93	0.91	1.29	58.86
E	0	20.32	17.19	0	0	62.49
F	14.51	5.00	22.97	1.33	1.42	54.77

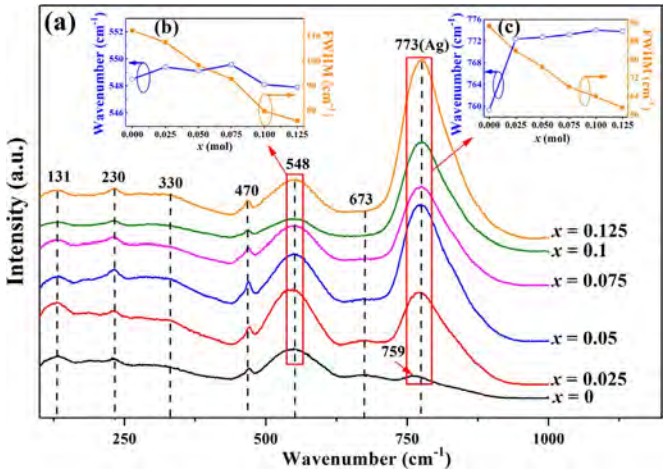

Fig. 5. (a) Raman spectra of CNT-CT*x* ceramics at sintered room temperature; (b) positions and FWHM of mode-5 (548 cm^{-1}) for CNT-CT*x* ceramics; (c) positions and FWHM of A_g mode (773 cm^{-1}) for CNT-CT*x* ceramics.

illustrated in Fig. 5(a), the spectrum consisted of seven distinguishable bands at 131, 230, 330, 470, 548, 673, and 759 cm^{-1}. The band at 759 cm^{-1} has been attributed to an A_g mode [34]. Balachandran et al. [35] attributed a band at approximately 673 cm^{-1} to the Ti–O stretching mode in their work on CT. The bands at 470 and 548 cm^{-1} were related to internal vibration of oxygen cage [32,35]. The bands in the region of 230–330 cm^{-1} may be assigned to the modes associated with rotations of the oxygen cage, and the band at 131 cm^{-1} was mainly due to the motion of A-site ions.

The results of Lorentzian fitting for Raman scattering spectra of CNT-CT*x* ceramics are shown in Fig. 6, which was to observe the changes in the Raman spectra of these samples with increase of *x* value. Moreover, Fig. 6 presents the modes positions and full width at half maximum (FWHM) of these modes. As shown in Fig. 5, compared to mode-5, the intensity of mode-7 (A_g) increased sharply as *x* increased. However, mode-6 disappeared at $x = 0.1$, 0.125, and this might be overlapped by excessively strong peak of mode-7. Fig. 5(b) illustrates positions and FWHM of mode-5 (548 cm^{-1}) in CNT-CT*x* ceramics. The FWHM of mode-5 decreased as *x* increased, and this finding indicated a stronger structural distortion of oxygen octahedra in CNT-CT*x* ceramics. In CNT-CT*x* ceramics, Cr^{3+} and Ta^{5+} ions were considered to occupy some Ti^{4+} ion at B-site. The different ionic sizes and force constants of Cr^{3+}, Ta^{5+} and Ti^{4+} may result in a nonequivalent configuration in two adjacent corner sharing oxygen octahedral, hence, the structural distortion of oxygen octahedra became stronger with increasing *x*. Additionally, as shown in Fig. 5(c), the position of A_g mode dramatically moved from 759.3 cm^{-1} at $x = 0$–772.4 cm^{-1} $x = 0.025$, which may be related to the cation disorder/order usually observed in $AB'_{1/3}B''_{2/3}O_3$ complex perovskites such as $Ba(Mg_{1/3}Nb_{2/3})O_3$ ceramic [36]. The substitution of Cr^{3+} and Ta^{5+} on the B-site may enhance the driving force for the short range order (SRO). As depicted in Fig. 5(c), the FWHM of A_g mode decreased with increasing Cr^{3+} and Ta^{5+} concentration, suggesting that the influence of SRO structure on Raman vibration peaks increased in crystal of CNT-CT*x* ceramics. SRO effects can be estimated by considering the visibly increasing intensity of A_g mode as *x* increased. Furthermore, their distribution should be affected by the differences of the charge and size among Cr^{3+}, Ta^{5+} and Ti^{4+} and the formation of the other phase ($Nd_2Ti_2O_7$, Ta_2O_5 and new unknown phase) at $x = 0.125$ in some way, then let to the change in the intensity of A_g mode.

3.3. Dielectric properties

Fig. 7(a) shows the relative density of CNT-CT*x* ceramics sintered at 1360–1450 °C. As presented in Fig. 7(a), there was a down trending for relative densities of all samples with increasing concentration of $(Cr_{0.5}Ta_{0.5})^{4+}$ ions, and relative densities decreased from 98% (at $x = 0$) to 93% (at $x = 0.125$). According to Fig. 4, Cr and Ta ions reduced the grain size of CNT-CT*x* samples, and the change of grain size had a major impact on the densification of CNT-CT*x* ceramics. During sintering, the decrease of grain size contributed to the formation of pores in the grain boundary. The existence of pores (as shown in Fig. 4(c)–(f)) was responsible for the decline of relative densities of samples.

It is well known that the relative permittivity (ε_r) depends on the relative density and the molecular polarizability to a certain extent. Fig. 7(b) shows the ε_r value of CNT-CT*x* ceramics sintered at different temperatures for 4 h. The ε_r value of CNT-CT*x* samples showed a declining trend similar to the relative density, decreasing from ~ 106 at $x = 0$ to ~ 81 at $x = 0.125$. Moreover, the molecular polarizability (α_m) is calculated according to the Shannon's additive rules [37] using the formula of $\alpha_m(\text{CNT-CT}x) = 0.61\alpha(Ca^{2+}) + 0.26\alpha(Nd^{2+}) + (1-x)\alpha(Ti^{4+}) + x/2[\alpha(Cr^{3+}) + \alpha(Ta^{5+})] + 3\alpha(O^{2-})$, and the results are shown in Table 1. As illustrated, the α_m value increased as *x* increased, because the value of $\alpha(Ta^{5+})$ (4.73 $Å^3$) is much larger than value of $\alpha(Ti^{4+})$ (2.93 $Å^3$). It was clear that the change of α_m value was opposite to that of the trend for ε_r value. As the analysis of Raman spectra above, the arrangement of Cr and Ta made oxygen octahedra distorted, then the coordination environment of B-site changed. The polarizability of the ions in crystal may be affected by the coordination environment [38], that is, the polarizability of ions was different before and after the formation of chemical bonds. Thus, the value of α_m increased with increasing *x*, whereas the ε_r value of CNT-CT*x* ceramics decreased. Moreover, as discussed above, the secondary phases ($Nd_2Ti_2O_7$ phase ($\varepsilon_r \sim 36$), Ta_2O_5 and unknown phase) were primarily responsible for the decline in the ε_r value when the $(Cr_{0.5}Ta_{0.5})^{4+}$ concentration exceeded 0.1. In conclusion, the decrease of ε_r value was attributed to the change in oxygen octahedra and to the vibration between the oxygen octahedra and the A-site cations, which directly influenced the effective ionic polarizabilities.

Fig. 7(c) presents the $Q \times f$ value of CNT-CT*x* ceramics sintered at different temperatures and the packing fraction of CNT-CT*x* ceramics sintered at 1420 °C vs the content of $(Cr_{0.5}Ta_{0.5})^{4+}$. In this work, the packing fraction was calculated using the Eq. (5) to find out the relationship between intrinsic loss and $Q \times f$ value of ceramics, and the corresponding data are listed in Table 1 and plotted in Fig. 7(c). As shown in Fig. 7(c), the $Q \times f$ value and packing fraction of CNT-CT*x* samples sintered at 1420 °C reached the maximum value at $x = 0.05$, but declined as *x* increased from 0.05 to 0.125. In the crystal, the anharmonic oscillation of atoms was affected by the space of the atomic vibration. For CNT-CT*x* ceramics, the increase of packing fraction was responsible for weakening anharmonic oscillation because the atomic vibration was restricted in a smaller space. Consequently, the $Q \times f$ value increased.

According to our previous work [39,40], the pure CNT ceramics had low $Q \times f$ value because the Ti^{4+} tended to transform into Ti^{3+} owing to the appearance of oxygen vacancies in high temperature. This mechanism could be expressed as following equation: $O_O^{\times} \rightarrow V_O^{\cdot\cdot} + 2e' + \frac{1}{2}O_2$, $e' + Ti^{4+} \rightarrow Ti^{3+}$. And the substitution of the

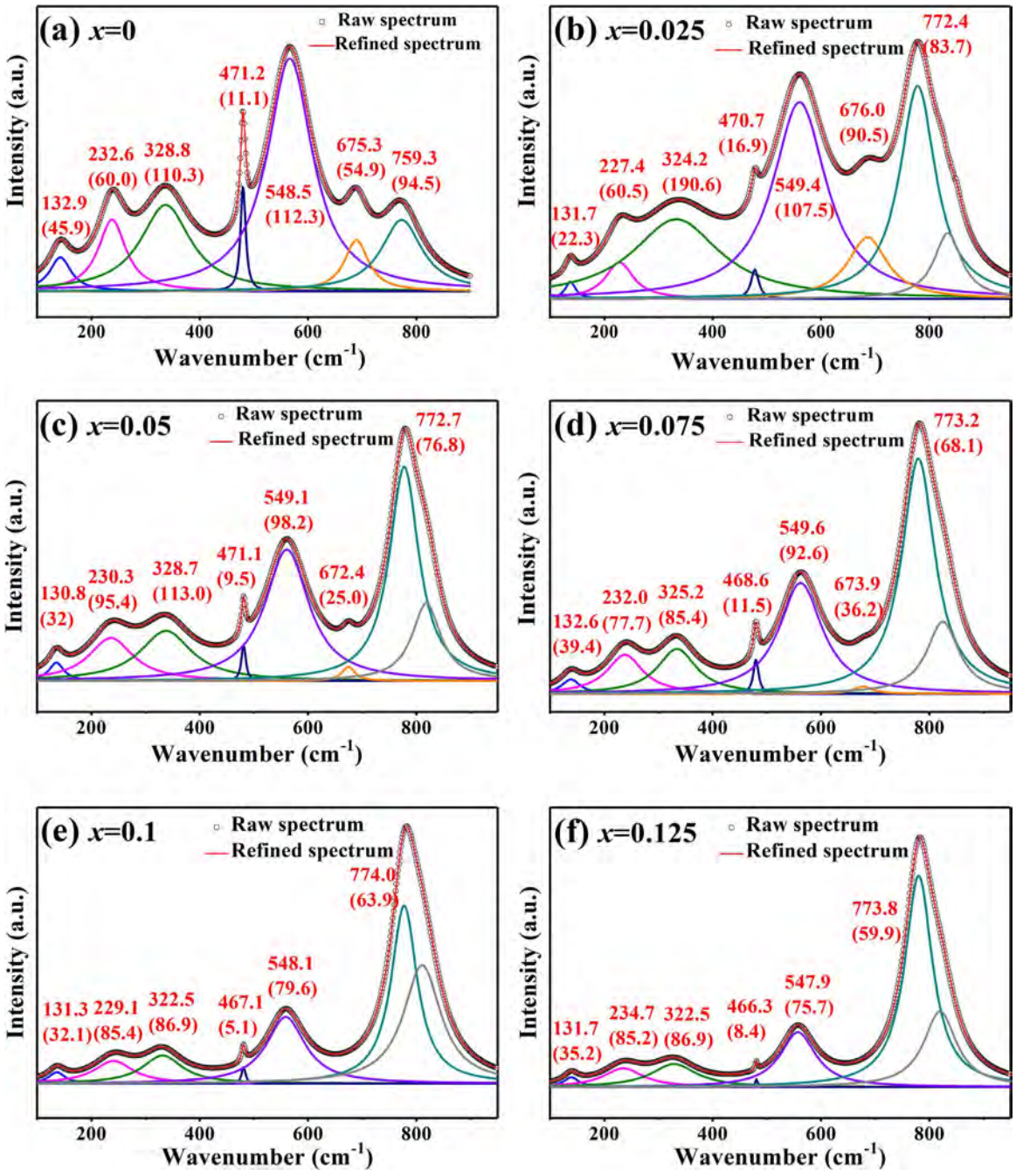

Fig. 6. Raman spectra of CNT-CTx ceramics sintered at 1420 °C for 4 h, fitted using Lorentzian functions with (a) x = 0; (b) x = 0.025; (c) x =0.05; (d) x = 0.075; (e) x = 0.1; (f) x = 0.125.

three-valence element Al and Cr for the four-valence element Ti restrained the Ti^{3+} accumulation by this reaction: $Cr_2O_3 \quad (Al_2O_3) \xrightarrow{TiO_2} 2Cr'_{Ti}(Al'_{Ti}) + V_O^{\bullet\bullet} + 3O_O^{\times}$. In addition, the XPS spectra of O-1s and Ti-2p core line for CNT-CTx (x = 0, 0.025, 0.05 and 0.075) ceramics are depicted in Figs. 8 and 9 respectively. The Ti-2p and O-1s region in CNT-CTx samples sintered at 1420 °C for 4 h were fitted well into the Gaussian sub peaks. The dominant peak at 529 eV (O1) was originated from the oxygen atoms bonded with nearest neighbor metal ion species (M–O) in the lattice, and the peak located at 530 eV (O2) was attributed to oxygen atoms in the vicinity of an oxygen vacancy [41,42]. The peak at around 531 eV was ascribed to the oxide in hydroxide (–OH), which included the absorption of oxygen on the surface of the CNT-CTx ceramics in the form H_2O and/or O_2 [43,44]. The Ti $2p_{3/2}$ and Ti $2p_{1/2}$ spin-orbital splitting photoelectrons of CNT-CTx ceramics were located at binding energies of around 458 and 464 eV, respectively. As shown in Figs. 8 and 9, the peak area of Ti $2p_{3/2}$ and oxygen vacancy (O2) varied with x value. So the surface fraction of oxygen vacancy (O2) and Ti^{3+} were estimated using the method proposed by Borchert et al. [45]. In this work, the ratio of the peak area of O2 to the peak area of M–O were defined as A_O, and the ratio of the peak area of Ti^{3+} to the peak area of Ti were defined as A_{Ti}. As shown in Figs. 8 and 9, the A_O and A_{Ti} value both decreased with increasing amount of Cr. Thus, the Cr dopant behaved as an effective suppressor of oxygen vacancy formation, and reduction of Ti^{4+} was suppressed accordingly. For microwave dielectric ceramics, microwave absorption of substance is caused by the conductive loss and dielectric relaxation loss of substance. If the oxygen vacancies decreased, the effect of weak-bound electron on conductivity became weak. Then the conductive loss

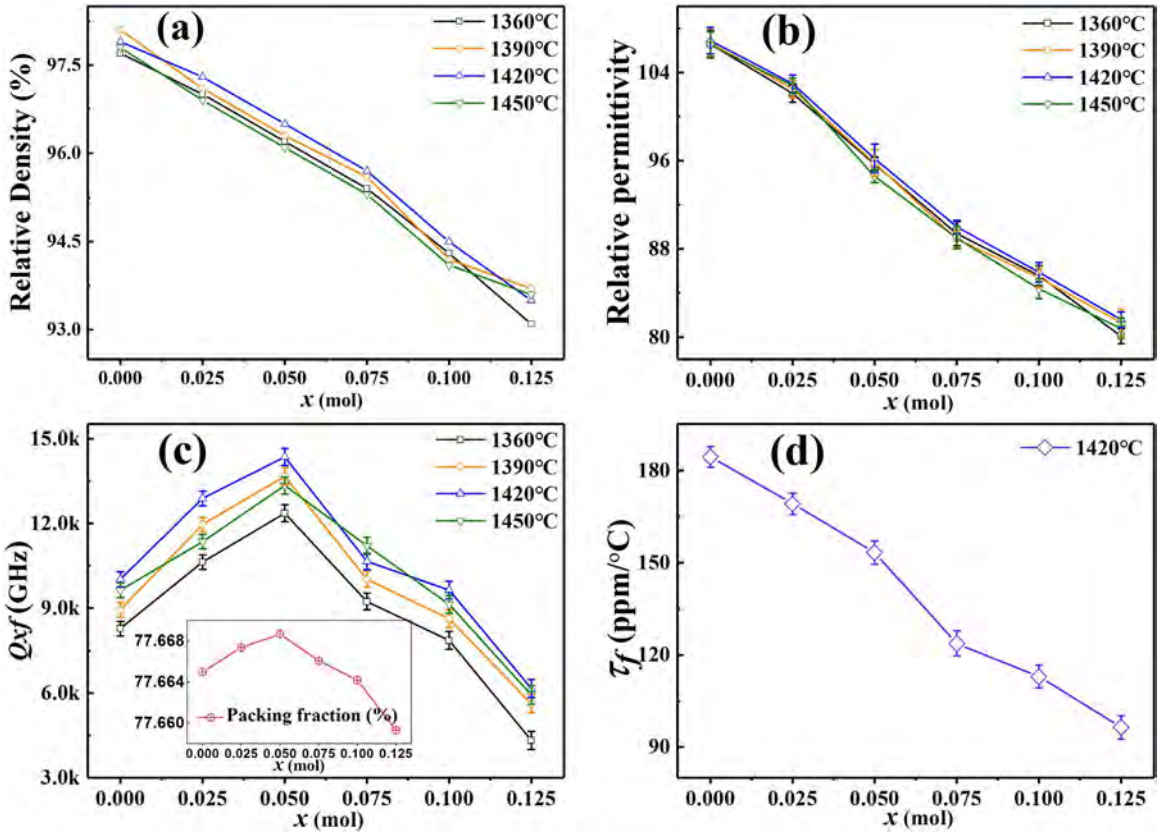

Fig. 7. Relative densities and microwave dielectric properties of CNT-CT*x* ceramics sintered at different temperature for 4 h with (a) relative density; (b) relative permittivity; (c) $Q \times f$ value; (d) temperature coefficient of resonant frequency (τ_f). Each error bar denotes the estimated standard deviation obtained from tests of microwave dielectric properties.

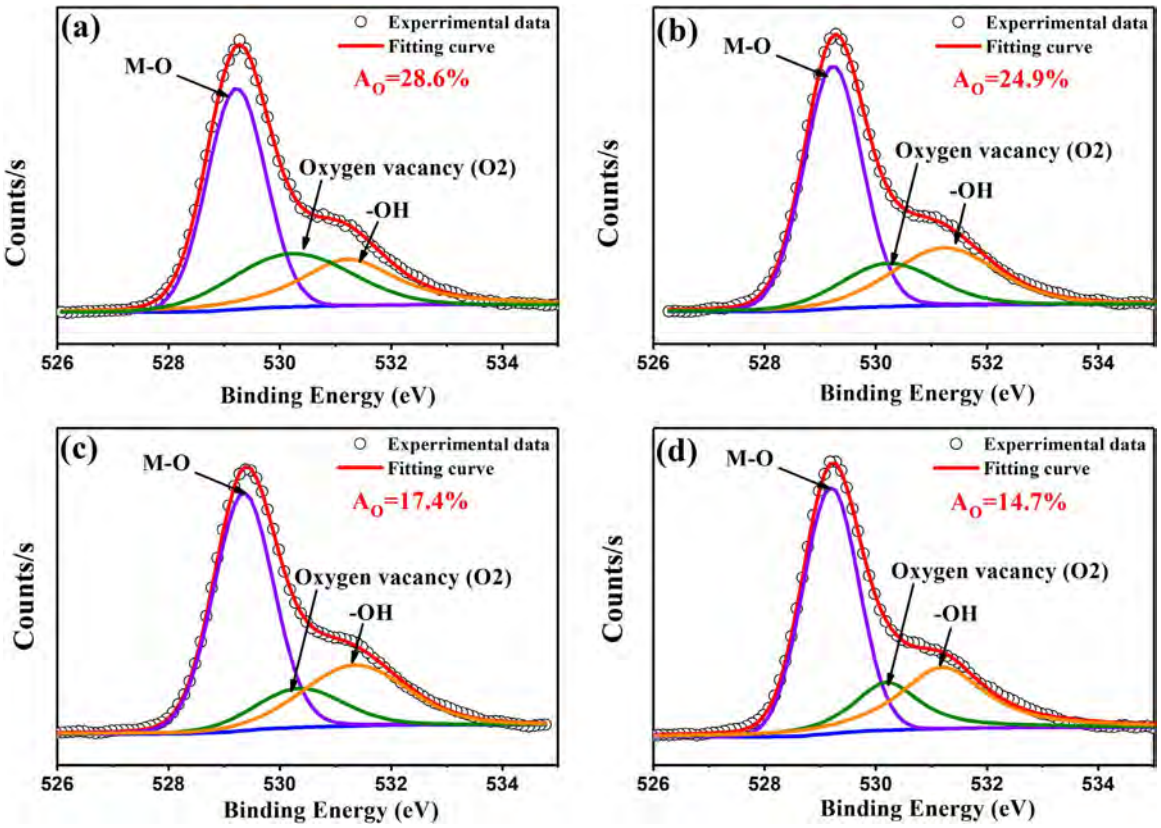

Fig. 8. XPS spectra of O-1s core line ranging for CNT-CT*x* ceramics sintered at 1420 °C for 4 h with (a) $x = 0$; (b) $x = 0.025$; (c) $x = 0.05$; (d) $x = 0.075$.

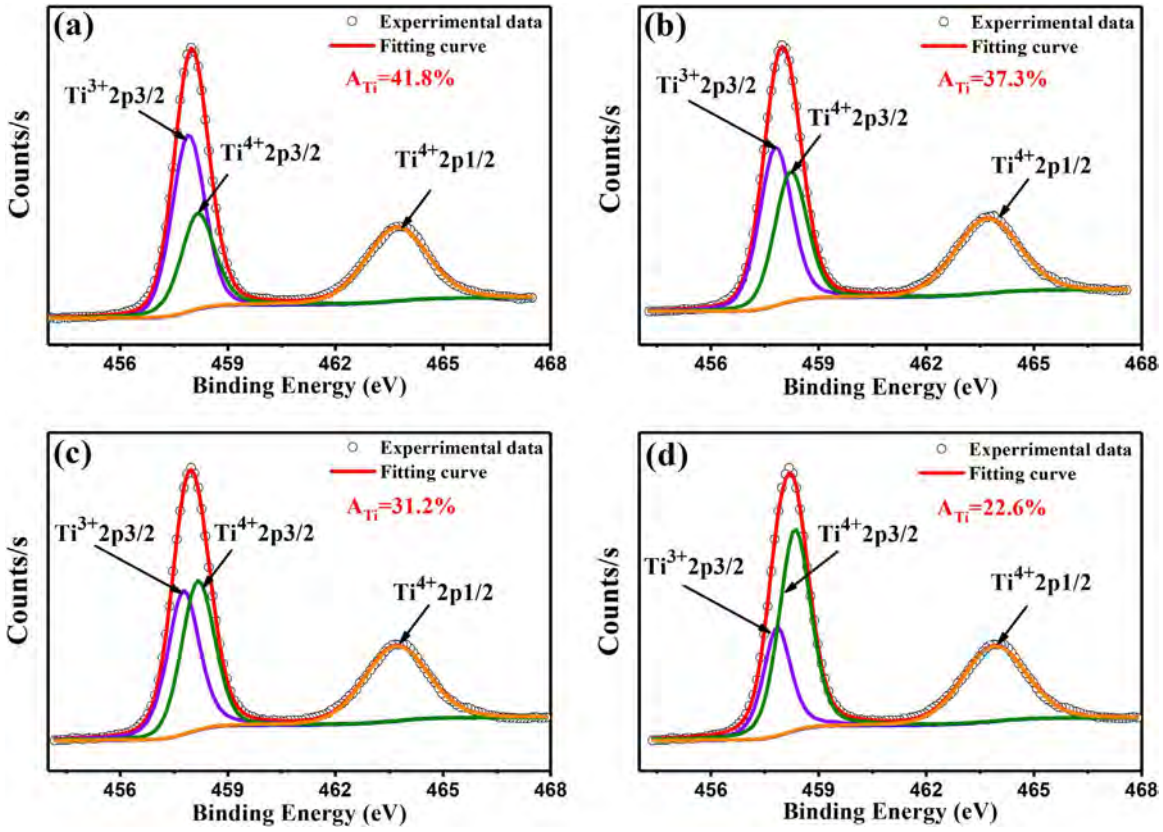

Fig. 9. XPS spectra of Ti-2p core line ranging for CNT-CTx ceramics sintered at 1420 °C for 4 h with (a) $x = 0$; (b) $x = 0.025$; (c) $x = 0.05$; (d) $x = 0.075$.

declined, finally leading to the improvement of $Q \times f$ value. As a result, when x was in the range from 0.075 to 0.125, SRO structures, distorted oxygen octahedral and the secondary phase should be a strong factor for the decline of $Q \times f$ value.

Fig. 7(d) shows the trend of τ_f of CNT-CTx ceramics sintered at 1420 °C for 4 h with increasing x value. Distinctly, the τ_f of CNT-CTx ceramics decreased towards the direction of the negative value when the concentration of $(Cr_{0.5}Ta_{0.5})^{4+}$ increased. As is well known, the τ_f is related to the temperature coefficient of permittivity (τ_ε) and the thermal expansion coefficient (α_L), as given in Eq. (6).

$$\tau_f = -(\frac{\tau_\varepsilon}{2} + \alpha_L) \tag{6}$$

Here, α_L is commonly a positive constant in ceramics. Eq. (6) demonstrated empirically that $\tau_f \propto -\tau_\varepsilon$ for dielectric materials. Colla et al. [46] derived an expression for τ_ε as Eq. (7).

$$\tau_\varepsilon = \frac{(\varepsilon-1)(\varepsilon+2)}{\varepsilon}(A + B + C) = \frac{(\varepsilon-1)(\varepsilon+2)}{\varepsilon}\left[\frac{1}{\alpha_m}(\frac{\partial\alpha_m}{\partial T})_V + \frac{1}{\alpha_m}(\frac{\partial\alpha_m}{\partial V})_T(\frac{\partial V}{\partial T})_P - \frac{1}{V}(\frac{\partial V}{\partial T})_P\right] \tag{7}$$

where α_m and V denote the polarizability and volume, respectively. The term A normally has negative value. For tilted octahedra structure, the term B and C are normally the largest ones and τ_ε depends mainly on them. In CNT-CTx ceramics, the substitution of $(Cr_{0.5}Ta_{0.5})^{4+}$ for Ti^{4+} gave rise to distorted oxygen octahedra and tend to have near zero or positive τ_ε. Conversely, the τ_f value would have a negative potential move according to Eq. (6). It is reported that τ_f is largely related to the recovery energy of structural distortion of oxygen octahedra [47,48]. In Ref [47 and 48], B-site bond valence has been applied to evaluate the τ_f of perovskite compounds. The B-site bond valence was calculated by using Eqs. (3) and (4) and Table 3 lists the B-site bond valence and τ_f of CNT-CTx ceramics sintered at 1420 °C for 4 h. As shown in Table 3, the

Table 3
B-site bond valence and τ_f of CNT-CTx ceramics sintered at 1420 °C for 4 h.

x	$R_{B\text{-}O}$	$d_{B\text{-}O}$	B	$V_{B\text{-}O}$	τ_f (ppm/°C)
0	1.815	1.91726	0.37	4.5512	184.5
0.025	1.81518	1.91728	0.37	4.5531	169.2
0.05	1.81535	1.91731	0.37	4.5548	153.3
0.075	1.81553	1.91737	0.37	4.5566	123.7
0.1	1.8157	1.91743	0.37	4.5577	112.9
0.125	1.81588	1.91751	0.37	4.5588	96.4

τ_f linearly decreased from 184.5 ppm/°C to 96.4 ppm/°C with increase of B-site bond valence. The larger bond valence usually means a stronger bond strength between oxygen and B-site ion with larger bond valence, and it also indicated that the τ_f values are affected by the interactions between the oxygen and cation such as tilted oxygen octahedra. Additionally, remarkable decrease of the τ_f value should be caused by the presence of $Nd_2Ti_2O_7$ phase due to its large negative τ_f value of −118 ppm/°C. As discussed above, the good and stable comprehensive properties of CNT-CT0.05 ceramics were obtained at 1420 °C: $\varepsilon_r = 96.5$, $Q \times f = 14{,}360$ GHz, $\tau_f = +153.3$ ppm/°C.

4. Conclusions

The CNT-CTx ceramics were prepared using the conventional solid-state method. The effects of substitution of $(Cr_{0.5}Ta_{0.5})^{4+}$ on the crystal structure, microstructure, Raman spectroscopy and microwave dielectric properties in CNT-CTx ceramics were investigated in detail. XRD analysis revealed that main phase of all samples were crystalized as an orthorhombic perovskite structure, and a single phase system was formed. But the impurity phases were found in the CNT-CT0.125 sample. The XRD peaks of (111), (131) and (311) implied super-reflections and they were originated from the antiphase tilting of oxygen

octahedra. SEM images showed that the average grain size increased with increasing sintering temperature, but it decreased with x value. According to Raman spectra, the substitution of Cr^{3+} and Ta^{5+} on the B-site enhanced the intensity of A_g mode, implying that SRO structure was formed in CNT-CTx ceramics. Also, the distortion of oxygen octahedra became stronger, and this finding was confirmed by changes of mode-5. From the analysis of XPS results, Cr^{3+} ion suppressed the reduction of Ti^{4+}, promoting the improvement of $Q \times f$ values for CNT-CTx ceramics in the range of 0–0.05. When content of $(Cr_{0.5}Ta_{0.5})^{4+}$ exceeded 0.075, the structured distortion not only contributed to the decrease of $Q \times f$ values, but led to the decrease of ε_r and τ_f value. Finally, CNT-CTx ceramics were obtained at 1420 °C with good and stable comprehensive properties of $\varepsilon_r = 96.5$, $Q \times f = 14{,}360$ GHz and $\tau_f = +153.3$ ppm/°C for $x = 0.05$.

Acknowledgement

This work is supported by the National Natural Science Foundation of China (Grant No. 51672038). In addition, Zhe Xiong wants to thank, in particular, the patience, care and support from Yuting Yin over the past years.

References

[1] F. Luo, B. Tang, Y. Yuan, Z. Fang, S. Zhang, Microstructure and microwave dielectric properties of $Na_{1/2}Sm_{1/2}TiO_3$ filled PTFE, an environmental friendly composites, Appl. Surf. Sci. 436 (2018) 900–906.

[2] Z. Xiong, B. Tang, C. Yang, S. Zhang, Correlation between structures and microwave dielectric properties of $Ba_{3.75}Nd_{9.5-x}Sm_xTi_{17.5}(Cr_{1/2}Nb_{1/2})_{0.5}O_{54}$ ceramics, J. Alloy. Compd. 740 (2018) 492–499.

[3] G. Chen, M. Hou, Y. Bao, C. Yuan, C. Zhou, H. Xu, Silver co-firable $Li_2ZnTi_3O_8$ microwave dielectric ceramics with LZB glass additive and TiO_2 dopant, Int. J. Appl. Ceram. Technol. 10 (2013) 492–501.

[4] G. Chen, J. Song, X. Kang, C. Yuan, C. Zhou, Improved discharged energy density for niobate-based B_2O_3 system glass–ceramics by CeO_2 addition, Mater. Lett. 136 (2014) 302–305.

[5] T. Zhang, R. Zuo, J. Zhang, Structure, microwave dielectric properties, and low-temperature sintering of acceptor/donor codoped $Li_2Ti_{1-x}(Al_{0.5}Nb_{0.5})_xO_3$ ceramics, J. Am. Ceram. Soc. 99 (2016) 825–832.

[6] Y. Masashi, H. Naoki, T. Takahiro, S. Akira, Structure and dielectric properties of $(Ca_{1-x}Nd_{2x/3})TiO_3$, Jpn. J. Appl. Phys. 36 (1997) 6818.

[7] C. Huiliang, H. Chengliang, Microwave dielectric properties and microstructures of $Ca_{1-x}Nd_{2x/3}TiO_3$–$Li_{1/2}Nd_{1/2}TiO_3$ ceramics, Jpn. J. Appl. Phys. 41 (2002) 5650.

[8] C. Zhou, G. Chen, Z. Cen, C. Yuan, Y. Yang, W. Li, Structure and microwave dielectric characteristics of lithium-excess $Ca_{0.6}Nd_{0.8/3}TiO_3$/$(Li_{0.5}Nd_{0.5})TiO_3$ ceramics, Mater. Res. Bull. 48 (2013) 4924–4929.

[9] C. Tseng, C. Huang, W. Yang, C. Hsu, Dielectric characteristics of $Nd(Zn_{1/2}Ti_{1/2})O_3$ ceramics at microwave frequencies, J. Am. Ceram. Soc. 89 (2006) 1465–1470.

[10] S.-Y. Cho, C.-H. Kim, D.-W. Kim, K.S. Hong, J.-H. Kim, Dielectric properties of Ln $(Mg_{1/2}Ti_{1/2})O_3$ as substrates for high-Tc superconductor thin films, J. Mater. Res. 14 (1999) 2484–2487.

[11] J. Li, C. Fan, S. Ran, Structure and microwave dielectric properties of (1–x)Nd $(Zn_{0.5}Ti_{0.5})O_3$–$xCa_{0.61}Nd_{0.26}TiO_3$ ceramics, Ceram. Int. 42 (2016) 607–614.

[12] M. Hu, H. Gu, X. Chu, J. Qian, Z. Xia, Crystal structure and dielectric properties of $(1-x)Ca_{0.61}Nd_{0.26}TiO_3 + xNd(Mg_{1/2}Ti_{1/2})O_3$ complex perovskite at microwave frequencies, J. Appl. Phys. 104 (2008) 124104.

[13] Y. Yan, Z. Li, M. Zhang, P. Sun, Y. Xu, Preparation and microwave dielectric properties of $Ca_{0.6}La_{0.8/3}(Sn_xTi_{1-x})O_3$ ceramics, Ceram. Int. 43 (2017) 8534–8537.

[14] F. Liu, C. Yuan, X. Liu, J. Qu, G. Chen, C. Zhou, Effects of structural characteristics on microwave dielectric properties of $(Sr_{0.2}Ca_{0.488}Nd_{0.208})Ti_{1-x}Ga_{4x/3}O_3$ ceramics, Mater. Res. Bull. 70 (2015) 678–683.

[15] J. Qu, F. Liu, C. Yuan, X. Liu, G. Chen, Microwave dielectric properties of $0.2SrTiO_3 - 0.8Ca_{0.61}Nd_{0.26}Ti_{1-x}Al_{4x/3}O_3$ ceramics, Mater. Sci. Eng. B 191 (2015) 15–20.

[16] M. Jong Ha, M.J. Hyun, S.P. Hyun, Y.S. Jong, S.K. Ho, Sintering behavior and microwave dielectric properties of (Ca, La)(Ti, Al)O_3 ceramics, Jpn. J. Appl. Phys. 38 (1999) 6821.

[17] F. Liang, M. Ni, W. Lu, S. Feng, Crystal structure and microwave dielectric properties of $CaTiO_3$–$La[Ga_{(1-\delta)}Al_\delta]O_3$ ceramics system, Mater. Res. Bull. 57 (2014) 140–145.

[18] R. Shannon, Revised effective ionic radii and systematic studies of interatomic distances in halides and chalcogenides, Acta Crystallogr. A 32 (1976) 751–767.

[19] N. Brese, M. O'keeffe, Bond-valence parameters for solids, Acta Crystallogr. Sect. B: Struct. Sci. 47 (1991) 192–197.

[20] M.R. Ian, L.C. Enrico, S. Nava, Dielectric and structural characteristics of Ba- and Sr-based complex perovskites as a function of tolerance factor, Jpn. J. Appl. Phys. 33 (1994) 3984.

[21] A. Glazer, The classification of tilted octahedra in perovskites, Acta Crystallogr. B 28 (1972) 3384–3392.

[22] A. Glazer, Simple ways of determining perovskite structures, Acta Crystallogr. A 31 (1975) 756–762.

[23] E. Brzozowski, M.S. Castro, C.R. Foschini, B. Stojanovic, Secondary phases in Nb-doped $BaTiO_3$ ceramics, Ceram. Int. 28 (2002) 773–777.

[24] Y.D. Hou, P.X. Lu, M.K. Zhu, X.M. Song, J.L. Tang, B. Wang, H. Yan, Effect of Cr2O3 addition on the structure and electrical properties of $Pb((Zn_{1/3}Nb_{2/3})_{0.20}(Zr_{0.50}Ti_{0.50})_{0.80})O_3$ ceramics, Mater. Sci. Eng. B 116 (2005) 104–108.

[25] R.B. Atkin, R.M. Fulrath, Point defects and sintering of lead zirconate-titanate, J. Am. Ceram. Soc. 54 (1971) 265–270.

[26] H. Yang, E. Li, S. Duan, H. He, S. Zhang, Structure, microwave properties and low temperature sintering of Ta_2O_5 and Co_2O_3 codoped $Zn_{0.5}Ti_{0.5}NbO_4$ ceramics, Mater. Chem. Phys. 199 (2017) 43–53.

[27] D.L. Rousseau, R.P. Bauman, S.P.S. Porto, Normal mode determination in crystals, J. Raman Spectrosc. 10 (1981) 253–290.

[28] Z. Fang, B. Tang, Y. Yuan, X. Zhang, S. Zhang, Structure and microwave dielectric properties of the $Li_{2/3(1-x)}Sn_{1/3(1-x)}Mg_xO$ systems (x = 0-4/7), J. Am. Ceram. Soc. 101 (2018) 252–264.

[29] Z. Xiong, B. Tang, Z. Fang, C. Yang, S. Zhang, Crystal structure, Raman spectroscopy and microwave dielectric properties of $Ba_{3.75}Nd_{9.5}Ti_{18-z}(Al_{1/2}Nb_{1/2})_zO_{54}$ ceramics, J. Alloy. Compd. 723 (2017) 580–588.

[30] H. Zheng, G.D.C. Csete de Györgyfalva, R. Quimby, H. Bagshaw, R. Ubic, I.M. Reaney, J. Yarwood, Raman spectroscopy of B-site order–disorder in $CaTiO_3$-based microwave ceramics, J. Eur. Ceram. Soc. 23 (2003) 2653–2659.

[31] H. Zheng, I.M. Reaney, G.D.C.C. de Györgyfalva, R. Ubic, J. Yarwood, M.P. Seabra, V.M. Ferreira, Raman spectroscopy of $CaTiO_3$-based perovskite solid solutions, J. Mater. Res. 19 (2004) 488–495.

[32] T. Hirata, K. Ishioka, M. Kitajima, Vibrational spectroscopy and X-ray diffraction of perovskite compounds $Sr_{1-x}M_xTiO_3$(M = Ca, Mg; $0 \le x \le 1$), J. Solid. State Chem. 124 (1996) 353–359.

[33] R. Lowndes, M. Deluca, F. Azough, R. Freer, Probing structural changes in $Ca_{(1-x)}Nd_{2x/3}TiO_3$ ceramics by Raman spectroscopy, J. Appl. Phys. 113 (2013) 044115.

[34] G.A. Smolensky, I.G. Siny, R.V. Pisarev, E.G. Kuzminov, Raman scattering in ordered and disordered perovskite type crystals, Ferroelectrics 12 (1976) 135–136.

[35] U. Balachandran, N.G. Eror, Laser-induced Raman scattering in calcium titanate, Solid. State Commun. 44 (1982) 815–818.

[36] I.G. Siny, R. Tao, R.S. Katiyar, R. Guo, A.S. Bhalla, Raman spectroscopy of Mg-Ta order-disorder in $BaMg_{1/3}Ta_{2/3}O_3$, J. Phys. Chem. Solids 59 (1998) 181–195.

[37] R.D. Shannon, Dielectric polarizabilities of ions in oxides and fluorides, J. Appl. Phys. 73 (1993) 348–366.

[38] M.W. Lufaso, Crystal structures, modeling, and dielectric property relationships of 2:1 ordered $Ba_3MM'_2O_9$ (M = Mg, Ni, Zn; M' = Nb, Ta) perovskites, Chem. Mater. 16 (2004) 2148–2156.

[39] Z. Fang, B. Tang, F. Si, S. Zhang, Low temperature sintering of high permittivity Ca-Li-Nd-Ti microwave dielectric ceramics with $BaCu(B_2O_5)$ additives, J. Alloy. Compd. 693 (2017) 843–852.

[40] Z. Fang, B. Tang, E. Li, S. Zhang, High-Q microwave dielectric properties in the $Na_{0.5}Sm_{0.5}TiO_3 + Cr_2O_3$ ceramics by one synthetic process, J. Alloy. Compd. 705 (2017) 456–461.

[41] Y. Jung, W. Yang, C.Y. Koo, K. Song, J. Moon, High performance and high stability low temperature aqueous solution-derived Li-Zr co-doped ZnO thin film transistors, J. Mater. Chem. 22 (2012) 5390–5397.

[42] B. Ullah, W. Lei, X.-H. Wang, G.-F. Fan, X.-C. Wang, W.-Z. Lu, Dielectric and ferroelectric behavior of an incipient ferroelectric $Sr_{(1-3x/2)}Ce_xTiO_3$ novel solid solution, RSC Adv. 6 (2016) 91679–91688.

[43] K. Kim, S.Y. Park, K.-H. Lim, C. Shin, J.-M. Myoung, Y.S. Kim, Low temperature and solution-processed Na-doped zinc oxide transparent thin film transistors with reliable electrical performance using methanol developing and surface engineering, J. Mater. Chem. 22 (2012) 23120–23128.

[44] E.M.C. Fortunato, L.M.N. Pereira, P.M.C. Barquinha, A.M.B.d. Rego, G. Gonçalves, A. Vilà, J.R. Morante, et al., High mobility indium free amorphous oxide thin film transistors, Appl. Phys. Lett. 92 (2008) 222103.

[45] H. Borchert, Y. Borchert, V.V. Kaichev, I.P. Prosvirin, G.M. Alikina, A.I. Lukashevich, V.I. Zaikovskii, et al., Nanostructured, Gd-doped ceria promoted by Pt or Pd: investigation of the electronic and surface structures and relations to chemical properties, J. Phys. Chem. B 109 (2005) 20077–20086.

[46] E.L. Colla, I.M. Reaney, N. Setter, Effect of structural changes in complex perovskites on the temperature coefficient of the relative permittivity, J. Appl. Phys. 74 (1993) 3414–3425.

[47] K.H. Yoon, W.S. Kim, E.S. Kim, Dependence of the octahedral bond valence on microwave dielectric properties of $Ca_{1-x}Sm_{2x/3}TiO_3$ ceramics, Mater. Sci. Eng. B 99 (2003) 112–115.

[48] K. Hyun Yoon, E. Soo Kim, J.-S. Jeon, Understanding the microwave dielectric properties of $(Pb_{0.45}Ca_{0.55})[Fe_{0.5}(Nb_{1-x}Ta_x)_{0.5}]O_3$ ceramics via the bond valence, J. Eur. Ceram. Soc. 23 (2003) 2391–2396.